Microwave synthesis: characterization and electrochemical properties of amorphous activated carbon-MnO_2 nanocomposite electrodes

A. Bello[a], O. O. Fashedemi[b,c], F. Barzegar[a], M. J. Madito[a], D. Y. Momodu[a], T. M. Masikhwa[a], J. K. Dangbegnon[a], and N. Manyala[a*]

[a]Department of Physics, Institute of Applied Materials, SARCHI Chair in Carbon Technology and Materials, University of Pretoria, Pretoria 0028, South Africa.

[b]Department of Chemistry, University of Pretoria, Pretoria 0002, South Africa.

[c]Department of Chemistry, Augustine University Ilara-Epe, Lagos 106103, Nigeria.

Corresponding Author: *Email address: ncholu.manyala@up.ac.za (N. Manyala)

Tel: +27 (0)12 420 3549, Fax: +27 (0)12 420 2516

Abstract

The green chemistry route (Microwave) has been used to produce nanocomposite materials based on activated carbon (AC) and manganese (Mn) oxide nanostructures. XRD analysis revealed that amorphous and crystalline oxide structures were synthesized. Morphological studies reveal rod-like α-MnO_2 for the pristine sample, while cubic Mn_3O_4 and irregular shaped MnO_2 structures were anchored on the AC substrate as revealed by the scanning electron microscopy (SEM) showing that the nanostructures were uniformly distributed on AC. The electrochemical tests of the composites as electrodes show that the amorphous AC-MnO_2 had a specific capacitance of 180 F g^{-1}, nearly four times higher than that of crystalline AC-Mn_3O_4 composite electrode (55 F g^{-1}). The Coulombic efficiency for the AC-MnO_2 cell was 98 % after 5000 cycles indicating a small capacitance loss. The green route technique and good electrochemical properties indicate that the amorphous AC-MnO_2 nanocomposite could be a good material for high-capacity, low-cost, and environmentally friendly electrodes for electrochemical capacitors.

Keywords: Amorphous activated carbon, MnO_2 nanostructure, Composites, Microwave irradiation, Electrochemical capacitor, Energy storage.

Introduction

Recently there has been a tremendous increase in potable and wearable electronic devices and this has left the energy sector with a key technological challenge of energy storage. There is growing interest in research activities directed towards the development of low-cost, high-power and high energy density electrochemical energy-storage devices to meet the increasing energy demand [1]. Supercapacitors are at the forefront of this research because of the rapid power delivery and long cycle life. Due to these advantages they have found applications in regenerative braking systems, electrical vehicles, portable electronic devices, and backup power [2]. However, the relatively lower energy density of supercapacitors when compared with that of batteries has thus limited their full potential and wide-spread application as primary energy storage devices [3]. The storage mechanism of supercapacitors can be classified into two namely: the electrical double layer capacitors (EDLCs) which store charges by rapid adsorption of electrolyte ions on high-surface-area electrode materials such as, onion-like carbons (OLCs), activated carbon (AC), graphene, carbide-derived carbons (CDCs) and carbon nanotubes (CNTs) [4–7] and the pseudocapacitors (Faradaic mechanism) that store and release charges in a Faradaic electron-transfer process [8]. Transition metal oxides (TMOs) and conducting polymers (polypyrrole) [9] are usually explored for pseudocapacitive applications. Many TMOs including RuO_2, [10] MnO_2, [11] Co_2O_3 [12], Co_3O_4 [13], NiO [14,15], Fe_3O_4 [16], TiO_2 [17], and V_2O_5 [18] have been tested as electrode materials. Amongst all these materials, RuO_2 and MnO_2 have been widely studied due to following properties: simple and scalable synthesis procedure, intrinsically high inherent pseudocapacitance, and rapid charging-discharging. However, the high cost and toxic nature of RuO_2 serves a major drawback for its commercialization and practical applications [19].

MnO_2 is a potentially interesting electroactive electrode material for electrolytic supercapacitors due to its low cost, natural abundance, low level of toxicity for humans, intrinsically high capacity in mild aqueous electrolytes and environmental compatibility [11]. Nevertheless, MnO_2 has limitations such as low surface areas, poor electrical conductivity, and poor cycling performance [11]. A variety of MnO_2 morphologies such as nanoparticles, flowerlike structure, spheres, nanorods, nanotubes have been achieved [11,20]. Additionally, different crystallographic phases (such as *α, β, γ, ε, δ*) have all been reported [21]. Carbon-based supercapacitors also show low charge storage capacity due to the limited electrolyte ions adsorption and desorption on the surface of the carbon [20]. To address this issue and improve the electrochemical

performance of carbon based materials to meet the demands for high-performance supercapacitors, intensive research efforts and effective strategy are being focused towards optimization of its electrochemical performance through incorporation of several TMOs with the different carbon materials with controlled micro/nanostructures to improve on the performance of the supercapacitors. The understanding of the synergistic effect, the design of integrated materials network architecture in which each component's properties play important role still needs to be optimized and a fast ion and electron transfer which guarantee efficient electrochemical performance still remains a great challenge.

Recently, three dimensional porous carbons (e.g. micro, meso and macroporous) have become attractive and it has inspired efforts to develop hybrids based on the incorporation of TMOs (such as MnO_2) into 3D porous network architecture which could be a promising method for enhancing its capacity of the composite materials [22–24]. Such hybrids material combined the merits of the double layer capacitance of the porous carbon and pseudocapacitance properties of MnO_2 materials which contribute to the total electrochemical capacitance value of the hybrid electrode material. Various composite materials based on conductive carbon materials such as carbon nanotubes (CNTs), activated carbon (AC) or graphene with nanostructured MnO_2 have been widely studied [25–27]. Under different synthesis modes, various shapes and morphology of MnO_2 nanostructures can be anchored on the given substrate (carbon).

As stated earlier, different synthesis technique give rise to different morphology of MnO_2 on the substrate material hence the development of high-performance hybrids-electrode based materials for energy-storage, requires the desirable structure and properties. In this regard, the synthesis method and microstructure properties are all important and play crucial role on the hybrid materials. In the present work, we have anchored manganese oxide nanostructure onto porous activated carbon materials using hydrothermal microwave irradiation. The formation mechanisms and evolution of the different nanostructures and the energy storage mechanism for electrochemical applications have been elucidated. The effect of composites materials on electrochemical performances, such as CV-curves, charge-discharge behaviours, electrochemical impedance spectroscopy (EIS), specific capacitance of the composite electrode and the dependency of the nanostructure on the electrochemical performance were tested and discussed in a two-electrode aqueous symmetric configuration.

Experimental

Activated carbon materials were prepared using a method in our previous work [28,29]. The AC-MnO_x composites were prepared using both solvothermal (Ethylene glycol (EG) and water) and hydrothermal (water) routes with microwave irradiation. 0.5 g of AC was dispersed in equal volumes of both mixed solvent and water respectively by ultrasonication. 0.26 grams of $KMnO_4$ was added to both mixtures while 1.5 ml of HCl was added drop wise to the aqua mixture only. Both solutions were stirred to obtain homogeneous mixtures after which they were transferred into separate quartz vessels in a microwave reactor (Anton Paar Synthos 3000 multimode reactor, 1400 W magnetron power) equipped with a wireless pressure and temperature sensor. The reactor was operated in the pressure mode using a power of 400 W. The temperature was ramped at 10 °C/minutes to 110 °C and kept constant at this temperature for 30 minutes, while the pressure was maintained at 80 bars throughout the hold period. After cooling the reaction chamber to room temperature, the resulting solid precipitates were collected and washed with deionized water and ethanol several times. The samples were then dried at 60 °C for 24 h. The obtained samples were designated as AC-Mn_3O_4 and AC-MnO_2 respectively.

Material characterization

Powder X-ray diffraction (XRD) was recorded in the 2θ range between 20.0 °–80.0 ° using an XPERT-PRO diffractometer (PANalytical BV, the Netherlands) with θ/2θ geometry and a counting time of 15.240 seconds per step. Qualitative phase analysis of samples was conducted with the X'pert Highscore search match software at room temperature using Co K1α (λ=0.178897 nm). Raman spectra of both samples were recorded using a WiTec-alpha 300R+ confocal Raman spectrometer (WiTec GmbH) with the laser power of 10 mW in order to minimize heating effects. The excitation source was a 532-nm laser through a numerical aperture of 0.9 and 20x magnification. Nitrogen adsorption-desorption isotherms were measured at −196 °C using a Micromeritics TriStar II 3020 (version 2.00). All the samples were degassed at 150 °C for more than 12 h under vacuum conditions. The surface area was calculated by the Brunauer–Emmett–Teller (BET) method from the adsorption branch in the relative pressure range (P/P_0) of 0.01 - 0.2. The SEM images were obtained on a Zeiss Ultra Plus 55 field emission scanning electron microscope (FE-SEM) operated at an accelerating voltage of 2.0 kV. The working electrodes for electrochemical evaluation were prepared by mixing 80 wt. % of the samples

with 10 wt. % carbon black and 10 wt. % polyvinylidene difluoride (PVdF) binder in an agate mortar. The mixture was then dissolved in 1-methyl-2-pyrrolidinone (NMP) to form a paste. The paste was coated on the Ni foam as a current collector with a diameter of 16 mm and dried at 60 $^{\circ}$C in an oven for 8 hours to ensure complete evaporation of the NMP. The weight of active material in each electrode with a diameter of 16 mm was at least 4 mg.

All of the electrochemical tests were investigated in a two-electrode configuration, with a glass microfiber filter paper as the separator in 1 M Na_2SO_4 aqueous electrolyte. The electrochemical properties of the devices were studied under room temperature and atmospheric pressure using cyclic voltammetry (CV), galvanostatic charge-discharge (GV) and electrochemical impedance was measured from 100 kHz to 0.01 Hz with zero potential amplitude using a Bio-logic SP-300 potentiostat driven by the EC-lab software.

Results and discussion

X-ray diffraction and Raman analysis

The pristine sample in the (supporting in information) shows the diffraction peaks typically observed in MnO_2 which are 12.8° (110), 18.1° (200), 28.8° (310), and 37.5° (211) [20]. The XRD analysis matched with JCPDS (00-044-0141) indicated the presence of α-MnO_2 with high intensity peaks corresponding to good crystallinity and high purity phase of the material. The X-ray diffraction (XRD) spectra taken from the powder of composite materials samples are shown in Fig. 1. The XRD pattern acquired from the composite when the mixture of water and ethylene glycol was used as solvent reveal the formation of crystalline trimanganese tetraoxide (Mn_3O_4) nanostructures. The patterns suggest that the addition of the AC in the presence of ethylene glycol gives rise to characteristic peaks of Mn_3O_4. The main product of the reduction of $KMnO_4$ in acidic medium is usually Mn^{4+} oxides in form of MnO_2 according to the reaction: . On the other hand, due to the presence of oxygen containing functional groups such as carboxyl, hydroxyl, epoxy and alkoxy groups produced as a result of the reduction of ethylene glycol in the solvent, we envisage the formation of other forms of manganese such as Mn^{2+} oxides -MnO- whose presence could further alleviate the formation Mn_3O_4 on the surface of the AC. Thus, the occurrence of a reaction of Mn^{3+} and Mn^{2+} oxides leads to the formation of Mn_3O_4 as represented in the following equation: . The AC-Mn_3O_4 composite obtained displayed diffraction peaks that match well with that of Mn_3O_4, spinel (JCPDS card, 01-089-4837). 2θ = 18°, 29°, 31°, 33°, 36°, 39°, 44°, 52°, 58°,

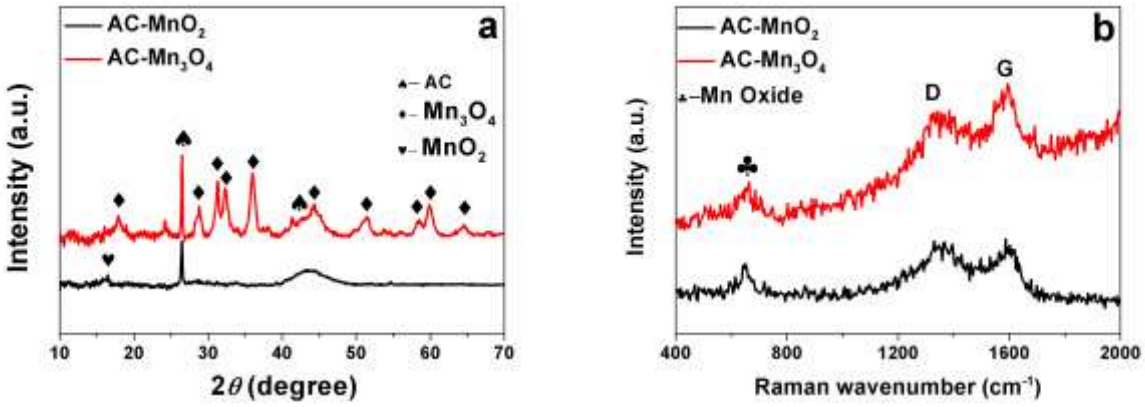

Figure 1 (a) XRD patterns and (b) Raman spectra of AC-MnO_2 and AC /Mn_3O_4

60°, and 64°, corresponding to peaks (101), (112), (200), (103), (211), (004), (220), (105), (321), (224) and (314) of Mn_3O_4 respectively [30]. The XRD pattern of the amorphous or poorly crystalline AC-MnO_2 shows very broad diffraction peaks that are generally identical to structures of MnO_2 (JCPDS card 00-008-0016). The intensity of the AC peaks supresses that of MnO_2 in the composite hence most of the peaks are in the background. The broad and low intensity XRD peaks indicate poor polycrystalline nature of the MnO_2. Additional peaks shown in the XRD pattern represented by the spade symbol signify the existence of AC in the samples, which clearly indicates the direct growth of Mn nanostructure on the AC surface. The addition of AC not only serves as the substrate for the growth of the nanostructures it also serves as a conductive agent to improve on the conductivity of the composite formed which can provide good electrochemical capacitance. Raman spectrum (Fig. 1 b) shows a peak at 630 cm^{-1} which is attributed to the Mn-O stretching vibration in the MnO_6 basal plane or the symmetric stretching vibration of the MnO_6 group [31]. The other two peaks at ~1590 cm^{-1} and at ~1350 cm^{-1}, are main features of graphitic carbon materials and are known as the G-band mode and the D-band mode (also known as disorder-induced band). The G-band originates from a normal first-order Raman scattering process in graphitic materials and the D-band from a second-order process that involves one iTO phonon and one defect [32]. The intensity of the G-band to the intensity of the D-band ($R=I_D/I_G$) for the AC-Mn_3O_4 was 0.98 and ~1.0 for the AC-MnO_2, indicating a low degree of graphitic crystalline structure

3.2 Scanning electron microscopy (SEM)

The FESEM images of the AC used as substrate for the composites materials and that of the pristine MnO_2 are shown in Fig. S2 of the supporting information. Fig. S2 a and b show low and high magnification images of the

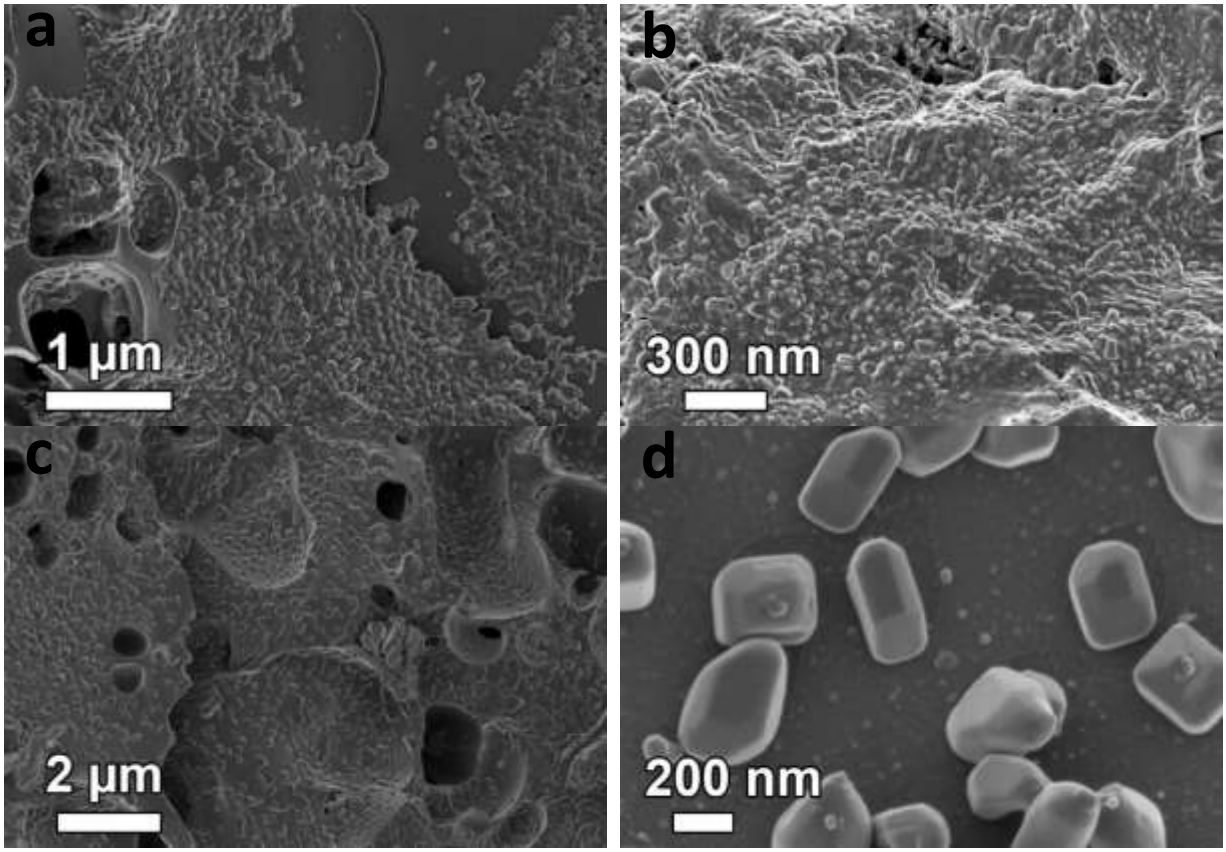

Figure 2 SEM micrographs of (a, b) AC-MnO_2 and (c, d) AC-Mn_3O_4

AC, while Fig. S2 c and d show low and high magnification images of the pristine MnO_2. The surface of the carbon substrate is covered with cavities which is an indication of the highly porous nature of the AC material. Fig S2 c and d also reveals typical high density rod like morphology obtained for pristine MnO_2. Higher magnification reveals a ≤ 120 nm thickness of the rods. Fig. 2 displays the FESEM micrographs of the two manganese oxide composites synthesised in this study. Fig. 2 a and b show the low and high magnification micrographs of the AC-MnO_2 composite with hydrothermal synthesis while Fig. 2 c and d show those of AC-Mn_3O_4 composite using solvothermal (mixed solvent of water and ethylene glycol) synthesis. Amorphous nanostructures of MnO_2 are seen to be evenly spread over the activated carbon in Fig. 2 a. A high magnification image (Fig. 2 b) shows that the nanostructures do not exhibit any particular shape when compared to the pristine MnO_2 which exhibited definite rod like structures. Their sizes are very different as the bigger particles are seen to be completely interspersed with smaller sized particles though the uniformity of their coverage all over the surface, orifices and pores of the AC substrate is quite distinguishable. Mn_3O_4 exhibited crystalline sub-micron sized particles which were also uniformly distributed on the AC substrate in Fig. 2 c. The good crystallinity of the particles may be attributed to the presence of EG which is a good absorber of microwave and could facilitate the reaction. A closer look at the composite in Fig. 2 d shows the

Mn_3O_4 particles are of various shapes. These micrographs are in agreement with the result obtained in XRD corroborating the amorphous and crystalline nature of the AC-MnO_2 and AC-Mn_3O_4 respectively. However, the variation in morphology is expected to affect the electrochemical performance of the two composite electrodes [33].

3.3 Gas sorption analysis

The specific surface area (SSA) of the composites were calculated by the Brunauer-Emmett-Teller (BET) method from the adsorption branch of the Nitrogen isotherms in the relative pressure range (P/P_0) of 0.01 - 0.2. The BET specific surface area of the AC substrate used in this study was 502 $m^2 g^{-1}$ [28]. The evolution of the different amorphous and polycrystalline structures of the manganese oxides on the AC substrate resulted in a drastic change in the surface area of the composite nanostructures. As shown in Fig. 3 a, the nitrogen adsorption and desorption isotherm curves exhibit typical type IV curves for both composite with H4 hysteresis loop signifying a complex mixture of both micro- and mesoporous materials. The BET specific surface area was found to be 449 90 and 290.29 $m^2 g^{-1}$ for AC-MnO_2 and AC-Mn_3O_4 respectively. The BJH pore size distribution shown in Fig. 3 b indicates the mesoporous nature of the materials. Inset to Fig. 3 b is the zoomed in images showing the presence of mesopores in the samples. The huge drop in SSA value of the AC-Mn_3O_4 sample is attributed to the formation of the various micron-sized structures during the microwave process. The values of the SSA could be correlated to the capacitance of each of the composites since the electrochemical performance of supercapacitive materials is highly dependent to pore distribution in their SSA for both electrochemical double layer and pseudocapacitive storage mechanism [20].

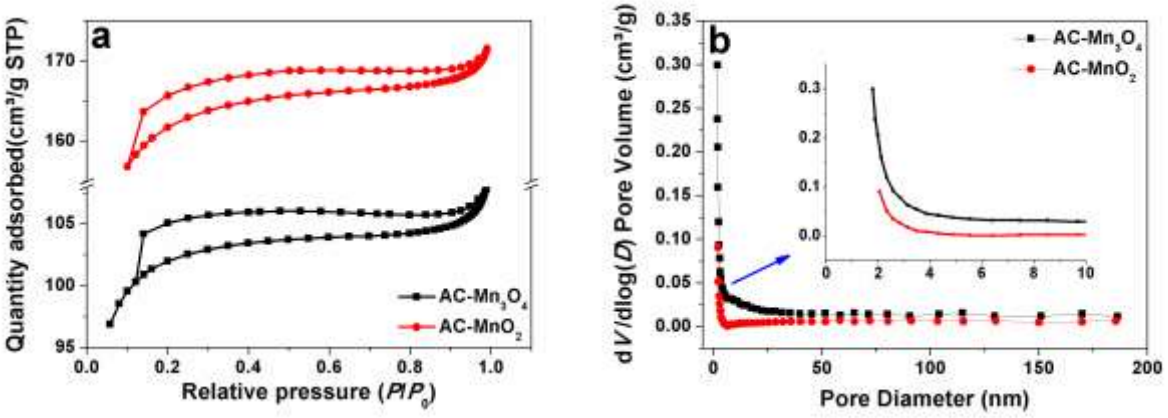

Figure 3 (a) N_2 adsorption/desorption isotherms and (b) BJH pore size distributions of AC-MnO_2 and AC-Mn_3O_4 respectively. Inset to Figure 3 (b) is the zoomed section of the figure indicated by the arrow showing the presence of mesopores in the samples.

Electrochemical characterisation

The electrochemical properties of the pristine MnO_2, AC-MnO_2 and AC-Mn_3O_4 were investigated using cyclic voltammetry (CV), galvanostatic charge-discharge (CD) and electrochemical impedance spectroscopy (EIS) experiments in 1 M Na_2SO_4 aqueous electrolyte in symmetric two electrode configuration. Fig. 4 shows the comparative CV profiles of the two electrodes at a scan rate of 20 mV s^{-1}. As seen from the CV curves (Fig. 4 a), the both electrodes exhibit nearly perfect symmetric rectangular shape which is indicative of ideal capacitors [1], however, there is a distinct difference between the current response in the CV spectra of AC-MnO_2 and AC-Mn_3O_4 as AC-MnO_2, shows a higher current response corresponding to the highest capacitance amongst the other two samples demonstrating more than twice the current response of AC-Mn_3O_4 and more that thrice that of pristine MnO_2 whose CV has a potential window of 0.8 V as shown in Fig. S3. This results Indicate that water is a good medium for synthesis of the nanostructure irrespective of the amorphous nature of the material. Since the AC-MnO_2 sample shows better electrochemical response, further exploration of the capacitive properties was made on the AC-MnO_2 cell. Galvanostatic charge-discharge (CD) measurements were performed to evaluate the rate performance of the electrodes materials. This was done by comparing their specific capacitance; calculated using the CD profile curves of the samples. Fig. 4 b shows typical CD profile of AC-MnO_2 and AC-Mn_3O_4 measured at a current density of 0.25 A g^{-1}. The highest discharge time was observed for AC-MnO_2 having more than thrice the value of AC-Mn_3O_4 and over a hundred times that of the pristine MnO_2 (Fig. S3). The galvanostatic discharge exhibited symmetric triangular profiles with specific capacitance of, 21.1, 33.31 and 181 F g^{-1} for α-MnO_2, AC-Mn_3O_4 and AC-MnO_2 respectively. Compared with other synthesis techniques that are available in the literature such as electrodeposition [34], hydrothermal autoclave [35], and reflux [36] for production of diverse Mn carbon based composites; the results obtained using the microwave approach are quite comparable and encouraging taking into account the reduced time for the synthesis of these materials by microwave. Fig. 4 c shows the cyclic voltammograms of this cell at scan rates ranging from 10-100 mV s^{-1} at a fixed voltage of 0.0-1.0 V. All the CV profiles recorded gave the quasi-rectangular resistive shapes with no deformation at increasing scan rates which characterised capacitance decay of the material at high sweep rates. Nevertheless, at 100 mV s^{-1} CV still exhibit double layer behavior suggesting excellent and efficient diffusion of charges at the electrode-electrolyte interfaces [4,37–39]. The good electrochemical character of this composite material can be attributed to the good and homogeneous

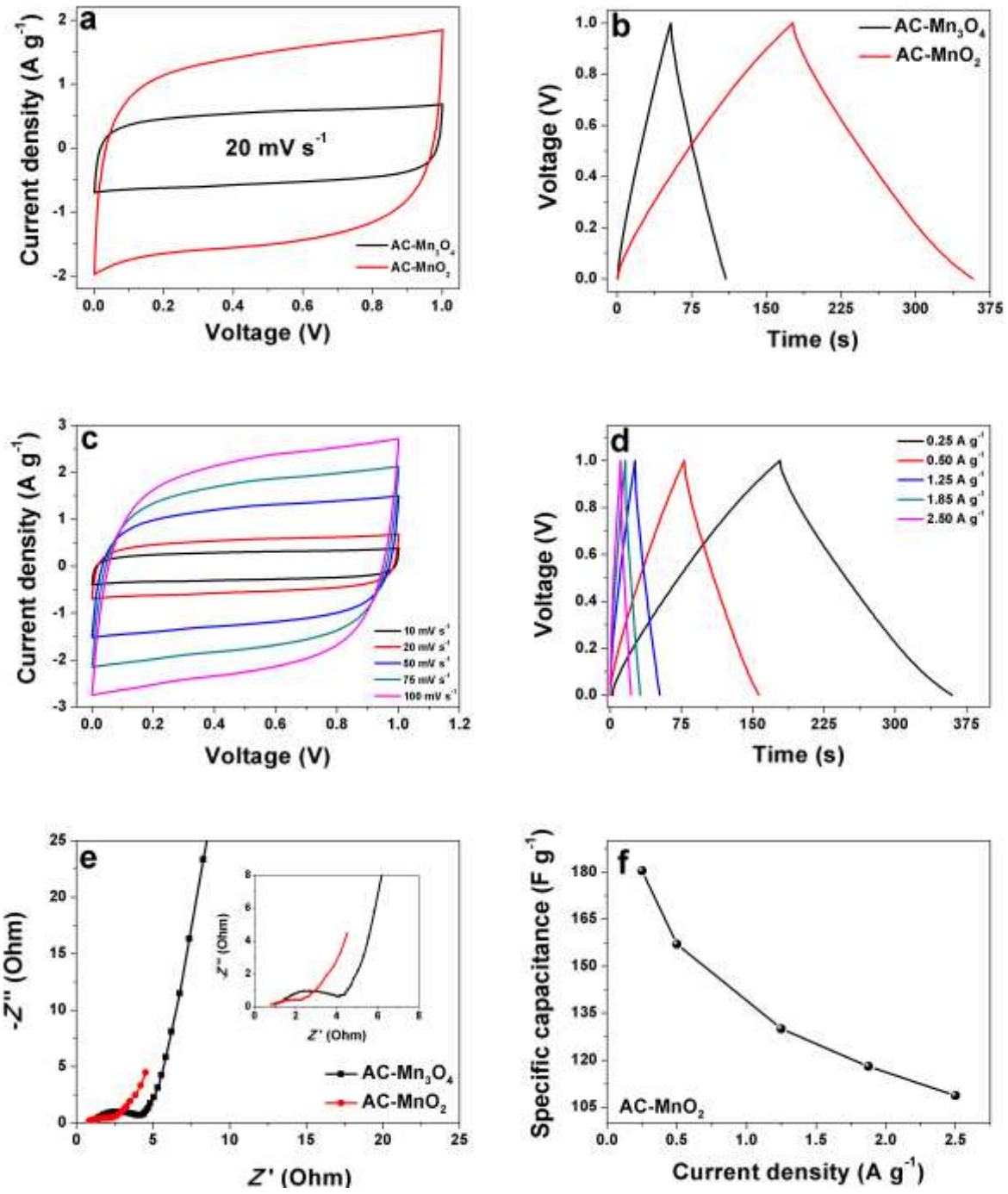

Figure 4 (a) comparison CV of AC-MnO_2 and AC /Mn_3O_4 at 20 mV s^{-1}, (b) CV profiles of AC-MnO_2 at different scan rates, (c) compares CD of AC-MnO_2 and AC /Mn_3O_4 at 0.25 A g^{-1}, (d) CD curves of AC-MnO_2 at different current densities and (e) Nyquist plot comparison and (f) specific capacitance as a function of current density for AC-MnO_2.

distribution of the MnO_2 nanostructures on the three dimensional interpenetrating network of the AC-material. Furthermore, the mesoporous texture and high surface area with adequate micropore volume and the conductivity of the AC substrate serves as the structural foundation for the high specific capacitance for this composite [40]. Table S1 gives the equivalent energy density and power density values of the three cells

measured at 0.25 A g^{-1} showing that the values of the amorphous material are far higher than the crystalline compounds

Although all the three samples have been synthesised using the same green microwave assisted technique, the AC-MnO_2 has consistently proved to be the best electrode material by yielding a higher specific capacitance and a better energy density value than the other two electrodes. This can be attributed to some of its distinctive physical properties such as its amorphous nature; which is in line with some previous studies that have suggested that the amorphous or poor crystalline manganese oxides with higher SSA are preferable as supercapacitor material [41–44]. Additionally the uniformity of its poor crystalline nanoparticle sizes allows for an even distribution of the nanoparticles on the AC surface. This has resulted in a complete coverage of the AC by the nano materials, the orifices of the porous AC can also be seen evenly aligned with the nanoparticles (SEM Fig. 2 b).The effect of this is noticeable in its larger BET specific surface area as stated above. Thus, its large accessible surface area facilitates a fast surface adsorption-desorption of the electrolyte ions on the electrode.

The CD curves at different current densities are shown in Fig. 4 d revealing linear voltage-time relation which is a characteristic of electric double layer capacitance. The resistance drop (IR drop) from the CD curves is very small and not noticeable, which suggests a smaller equivalent series resistance (*ESR*) value as will be discussed in the impedance analysis. Specific capacitance (C_{sp}), maximum energy (E_{max}) and power (P_{max}) densities of the cell were calculated from the CD curves using the conventional equation below:

$$C_{sp} = 4 \times I\,\Delta t / m\,\Delta V \quad (1)$$

$$E_{max} = 0.5\,C(\Delta V)^2 = (C_{sp} \times \Delta V^2)/28.8 \quad (2)$$

$$P_{max} = 3.6 \times E_{max}/\Delta t \quad (3)$$

where *I* is the discharge current (A), *m* is the total mass of the active material in both electrodes (g), Δt is the discharge time (s), ΔV is the applied potential (V).

The result shows that at high current density, the specific capacitance decrease, while higher capacitance values are at low current. At high current density, there is intercalation of ions at the surface of the active materials at the electrode/electrolyte interface, thus resulting in decrease of the specific capacitance. On the

other hand, at low current the specific capacitance increases due to the intercalation/de intercalation of ions at surface and inner porous of the active materials in the electrode/electrolyte interface [44]. The energy (*E*) and power (*P*) densities were calculated according to the equations above and their values are listed in table S1. The AC-MnO_2 cell had E_{max} of 7.53 Wh Kg^{-1} at 0.25 A g^{-1} with a value of 4.142 Wh Kg^{-1} at 2.25 A g^{-1}. Considering the symmetric nature of the cell, coupled with poor crystalline and amorphous nature of the material, these results are comparable to those reported for other manganese based electrodes with asymmetric configurations and operating at a higher potential window. Wang et al recorded an E_{max} value of 10.4 Wh Kg^{-1} using α-MnO_2//AC at 1.8 V [45] while Khomenko et al obtained an E_{max} value of 7.37 Wh Kg^{-1} using a composite of α-MnO_2/CNTs//PPY/CNT composite at 1.4 V [46]. It is worth stating that the composite were produced with other techniques rather the microwave approach.

The results from electrochemical Impedance spectroscopy provided further proof of the enhanced and superior capacitance of AC-MnO_2. As seen in Fig. 4 e, Nyquist plots of both nanocomposites exhibited a semicircle over the higher frequency range, followed by a linear part in the low frequency region. At high frequencies, the intercept at the real part (*Z'*) represents the values of the ohmic resistance of the electrolyte and the internal resistance (R_S) of the electrode known as the *ESR*. The R_S was found to be 6.0 Ω, for α-MnO_2 (Fig. S3), 1.0 Ω and 0.8 Ω, for AC-Mn_3O_4 and AC-MnO_2 respectively. Considering the fact that metal oxides are generally known to have poor electron conductivity [47–49] the higher R_S value for α-MnO_2 is not surprising. On the other hand, the presence of AC possessing relatively good electron conductivity is expected to enhance the conductivity of both AC-Mn_3O_4 and AC-MnO_2. Thus the lower R_S values obtained for the two composites indicates a small ion transfer resistance for both electrodes. The semi circles in the mid frequency are a measure of charge transfer resistance (R_{CT}) and the double capacitance (C_{dl}) in the composite material. In the mid frequency region a small semi-circle observed from the electrode is indicative of a low interfacial charge-transfer resistance (R_{CT}) while a vertical line in the low frequency region is indication of an electrode close to an ideal capacitor [50,51]. The R_{CT} values are 4.3 Ω for α-MnO_2, 3.66 Ω and 1.55 Ω for AC-Mn_3O_4 and AC-MnO_2 respectively. The large difference in the R_{CT} values of AC-Mn_3O_4 and AC-MnO_2 can be due to the resistance resulting from the frequency dependence of ion transport in the electrolyte. The slope of the 45° portion of the Nyquist plots is called the Warburg resistance (Z_w) and is as a result of the frequency dependence of ion diffusion or transport in the electrolyte to the electrode surface. The increase in the impedance of this region

indicates greater variations in the ion diffusion path lengths and the increase obstruction of ion movement [52,53]. Thus, the longer diffusion path length of AC-Mn_3O_4 (Fig. 4 e) could be attributed to the high charge density resulting in higher *ESR*. On the other hand AC-MnO_2 exhibited a very short diffusion path length of ions in the electrolyte which could be seen by its lesser R_S value. The specific capacitance as function of the current density of the AC-MnO_2 cell is shown in Fig. 4 f. The specific capacitance decreases from 180 F g^{-1} to 109 F g^{-1} with increasing current density retaining about 60% of its initial capacitance. The electrochemical results of the AC-Mn_3O_4 are shown in Fig. S4 in the supporting information.

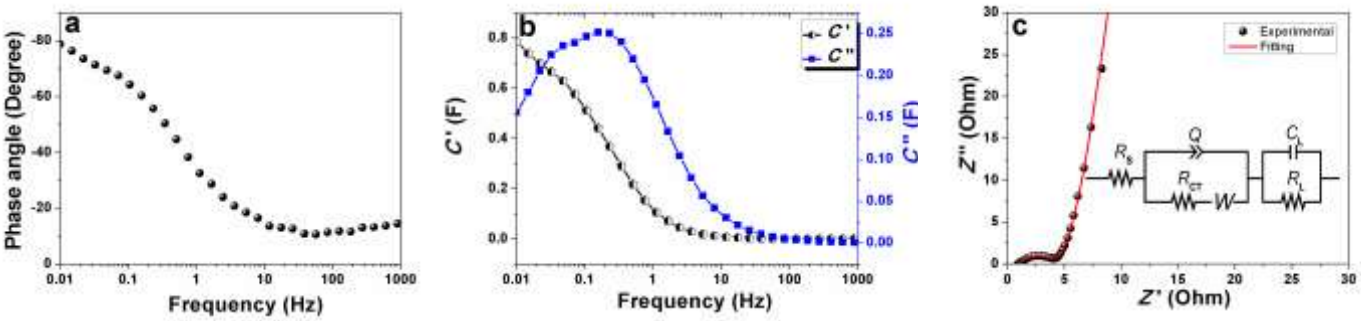

Figure 5 (a) Bode plot and (b) the real and imaginary capacitance against frequency of AC-MnO_2 (c) EIS plot and fitting data for the electrode with the equivalent circuit used for fitting the data as inset to the figure.

The profile of the impedance phase angle dependence on frequency-Bode plot is shown in Fig. 5 a for AC-MnO_2 sample. The phase angle is 80° at lower frequency region which close to an ideal capacitance which exhibits a phase angle of 90°. This further confirms the good capacitive property of the cell. The real and imaginary part (*C*' and *C*'') of the specific capacitance as a function of the frequency is shown in Fig 5 b. In the low frequency region, the capacitance (*C* (ω)) can be defined as the combination of imaginary part of the capacitance, (*C*'' (ω)) and the real part of the capacitance (*C*' (ω)); these are expressed by the equations below:

$$C = -1/\omega Z^{"} \quad (1)$$

$$C'(\omega) = \frac{-Z"(\omega)}{\omega|Z(\omega)|^2} \quad (2)$$

$$C^{"}(\omega) = \frac{Z"(\omega)}{\omega|Z(\omega)|^2} \quad (3)$$

Where (*C*'(ω)) corresponds to the static capacitance which is tested during the constant current discharge, (*C*''(ω)) corresponds to the energy dissipation of the supercapacitor by IR drop and an irreversible faradaic discharge transfer process which can cause the hysteresis of the electrochemical process. $|Z(w)|$ is the

impedance modulus, and ω is the angular frequency [15,54,55]. The evolution of ($C''(\omega)$ vs. frequency as seen in Fig. 5 b reaches a maximum at a frequency (f_r) of 0.15 Hz. This is the relaxation frequency and it represents the minimum time needed to discharge all the energy from the device with an efficiency of >50 % [56]. It also determines the relaxation time constant (τ_r) which is a quantitative measure of how fast the device can be charged and discharged reversibly and is expressed as: $\tau_r = 1/(2\pi f_r)$ [15]. τ_r was found to be 6 s thus exhibiting a faster charge - discharge time. Fig. 5 c shows the fitting of the EIS and the equivalent circuit diagram (inset to Fig. 5 c). The EIS data fitting was performed using a (ZFIT) software that applies the complex nonlinear least-squares (CNLS) method [8]. The equivalent series resistance R_S, is in series with the constant phase element, Q. The semi-circular arc in the high-frequency region to mid-frequency is modelled by a charge transfer resistance R_{CT} and Q which is responsible for the double layer capacitance of the cell. The R_{CT} describes the rate of redox reactions that might occur at the electrode-electrolyte interface [57]. The R_S and R_{CT} data obtained from the fitting fit well with the experimental data implying the model used for the fitting is reliable with an optimized minimization of experimental data with an error of 0.1. As stated earlier, the vertical line in the low-frequency region of the Nyquist plot represents the diffusion of ions to the interface between electrode and electrolyte. The deviation from the ideal vertical behavior is ascribed to the presence of resistance with a Warburg impedance characteristic element denoted by W, which is expressed as $A/(j\omega)^{0.5}$, [58] where A is the Warburg coefficient, ω is the angular frequency. The mass capacitance denoted by C_L is in parallel with the leakage current R_L which are all in series with R_S.

Cycling performance is another crucial factor in testing EDLC, [48] thus the long term stability of the symmetric cell of AC-MnO_2 was evaluated by repeating CD cycles at a current density of 1.25 A g^{-1} for 5000 cycles. The columbic efficiency as a function of cycle number, expressed in the equation below is shown in Fig. 6 a.

$$\varepsilon = t_d/t_c \times 100$$

where t_d is the discharge time and t_c is the charging time.

It can be seen from the figure that there was slight decrease at the beginning of cycles but it stabilises and this stability was kept throughout the duration of test. At the end of 5000 cycles, 99 % columbic efficiency was maintained. Cyclic voltammograms and EIS spectra of the cell before and after the 5000 cycles are shown in Figs. 6 b and c for comparison purposes. As can be observed, similar CV profiles were obtained before and

after the cycles with little capacitance loss. On the other hand there is a little increase in the R_S and R_{CT} values obtained from the Impedance spectra after the stability test. The slight increase is ascribed to increase in diffusion path length as observed in the spectra after cycling. All of these show that the AC-MnO_2 cell is highly stable.

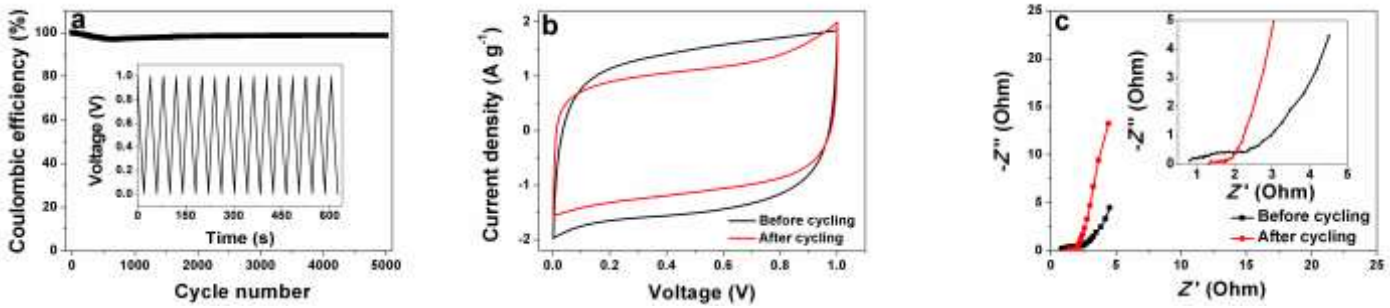

Figure 6 (a) Coulombic efficiency at a current density 1.25 A g^{-1}, (b) CV comparison before and after cycling and (c) EIS analysis before and after cycling of AC-MnO_2 cell.

CONCLUSION

Manganese oxide nanostructures have been synthesized by the green chemistry method (Microwave). Through the X-ray diffraction analysis, the different structures were identified. The AC-MnO_2 composite showed a promising eco-friendly candidate for EDLC electrode due to its higher surface area compared with the AC-Mn_3O_4 sample which could facilitates free access of electrolyte ions to the electrode surface (fast surface sorption processes), the uniform dispersal of the nanoparticles throughout the surface of the porous and conductive AC also reduces the diffusion length of ions within the pseudocapacitive phase, ensuring efficient utilization of the active materials, its good cycle stability is also an asset as it retains almost 98 % efficiency after 5000 cycles.

ACKNOWLEDGEMENT

"This work is based on the research supported by the South African Research Chairs Initiative of the Department of Science and Technology and National Research Foundation of South Africa (Grant No 97994). Any opinion, finding and conclusion or recommendation expressed in this material is that of the author(s) and the NRF does not accept any liability in this regard". A. Bello acknowledges NRF through SARChI in Carbon Technology and Materials and University of Pretoria for Postdoctoral and PhD financial support.

REFERENCES

[1] P. Simon, Y. Gogotsi, B. Dunn, Where do batteries end and supercapacitors begin?, Sci. Mag. 343 (2014) pp–1210.

[2] R. Liu, J. Duay, S.B. Lee, Heterogeneous nanostructured electrode materials for electrochemical energy storage, Chem. Commun. 47 (2011) 1384–1404.

[3] P. Simon, Y. Gogotsi, Materials for electrochemical capacitors, Nat. Mater. 7 (2008) 845–854.

[4] M. Inagaki, H. Konno, O. Tanaike, Carbon materials for electrochemical capacitors, J. Power Sources. 195 (2010) 7880–7903.

[5] P. Simon, Y. Gogotsi, Charge storage mechanism in nanoporous carbons and its consequence for electrical double layer capacitors, Philos. Trans. R. Soc. A Math. Phys. Eng. Sci. 368 (2010) 3457–3467.

[6] V. Presser, M. Heon, Y. Gogotsi, Carbide-Derived Carbons-From Porous Networks to Nanotubes and Graphene, Adv. Funct. Mater. 21 (2011) 810–833.

[7] P. Simon, Y. Gogotsi, Capacitive energy storage in nanostructured carbon--electrolyte systems, Acc. Chem. Res. 46 (2012) 1094–1103.

[8] B.E. Conway, Electrochemical Supercapacitors Scientific Fundamentals and Technological Applications Kluwer Academic/Plenum: New York, 1999.

[9] D. Zhang, X. Zhang, Y. Chen, P. Yu, C. Wang, Y. Ma, Enhanced capacitance and rate capability of graphene/polypyrrole composite as electrode material for supercapacitors, J. Power Sources. 196 (2011) 5990–5996.

[10] Z.-S. Wu, D.-W. Wang, W. Ren, J. Zhao, G. Zhou, F. Li, H-M. Cheng, Anchoring Hydrous RuO_2 on Graphene Sheets for High-Performance Electrochemical Capacitors, Adv. Funct. Mater. 20 (2010) 3595–3602.

[11] W. Wei, X. Cui, W. Chen, D.G. Ivey, Manganese oxide-based materials as electrochemical supercapacitor electrodes., Chem. Soc. Rev. 40 (2011) 1697–721.

[12] X.-C. Dong, H. Xu, X.-W. Wang, Y.-X. Huang, M.B. Chan-Park, H. Zhang, L-H Wang, W Huang, P. Chen, 3D graphene-cobalt oxide electrode for high-performance supercapacitor and enzymeless glucose detection., ACS Nano. 6 (2012) 3206–13.

[13] S.K. Meher, G.R. Rao, Effect of microwave on the nanowire morphology, optical, magnetic, and pseudocapacitance behavior of Co_3O_4, J. Phys. Chem. C. 115 (2011) 25543–25556.

[14] A. Bello, K. Makgopa, M. Fabiane, D. Dodoo-Ahrin, K.I. Ozoemena, N. Manyala, Chemical adsorption of NiO nanostructures on nickel foam-graphene for supercapacitor applications, J. Mater. Sci. 48 (2013) 6706–6712.

[15] D. Wang, W. Ni, H. Pang, Q. Lu, Z. Huang, J. Zhao, Preparation of mesoporous NiO with a bimodal pore size distribution and application in electrochemical capacitors, Electrochim. Acta. 55 (2010) 6830–6835.

[16] N. Nagarajan, I. Zhitomirsky, Cathodic electrosynthesis of iron oxide films for electrochemical supercapacitors, J. Appl. Electrochem. 36 (2006) 1399–1405.

[17] X. Lu, G. Wang, T. Zhai, M. Yu, J. Gan, Y. Tong, Y Li, Hydrogenated TiO_2 nanotube arrays for supercapacitors., Nano Lett. 12 (2012) 1690–6.

[18] S.D. Perera, B. Patel, N. Nijem, K. Roodenko, O. Seitz, J.P. Ferraris, Y.J. Chabal, K. J. Jr. Balkus, Vanadium Oxide Nanowire-Carbon Nanotube Binder-Free Flexible Electrodes for Supercapacitors, Adv. Energy Mater. 1 (2011) 936–945.

[19] H. Xia, Y. Shirley Meng, G. Yuan, C. Cui, L. Lu, Y.S. Meng, A symmetric RuO_2/RuO_2 supercapacitor operating at 1.6 V by using a neutral aqueous electrolyte, Electrochem. Solid-State Lett. 15 (2012) A60–A63.

[20] W. Chen, R.B. Rakhi, Q. Wang, M.N. Hedhili, H.N. Alshareef, Morphological and Electrochemical Cycling Effects in MnO_2 Nanostructures by 3D Electron Tomography, Adv. Funct. Mater. 24 (2014) 3130–3143.

[21] T.T. Truong, Y. Liu, Y. Ren, L. Trahey, Y. Sun, Morphological and crystalline evolution of nanostructured MnO_2 and its application in lithium-air batteries, ACS Nano. 6 (2012) 8067–8077.

[22] M. Liu, L. Gan, W. Xiong, Z. Xu, D. Zhu, L. Chen, Development of MnO_2/porous carbon microspheres with a partially graphitic structure for high performance supercapacitor electrodes, J. Mater. Chem. A. 2 (2014) 2555–2562.

[23] Y. Zhao, M. Liu, L. Gan, X. Ma, D. Zhu, Z. Xu, L Chen, Ultramicroporous carbon nanoparticles for the high-performance electrical double-layer capacitor electrode, Energy & Fuels. 28 (2014) 1561–1568.

[24] M. Liu, J. Qian, Y. Zhao, D. Zhu, L. Gan, L. Chen, Core-shell ultramicroporous@ microporous carbon nanospheres as advanced supercapacitor electrodes, J. Mater. Chem. A. 3 (2015) 11517–11526.

[25] J. Yan, Z. Fan, T. Wei, W. Qian, M. Zhang, F. Wei, Fast and reversible surface redox reaction of graphene–MnO_2 composites as supercapacitor electrodes, Carbon 48 (2010) 3825–3833.

[26] R.B. Rakhi, D. Cha, W. Chen, H.N. Alshareef, Electrochemical energy storage devices using electrodes incorporating carbon nanocoils and metal oxides nanoparticles, J. Phys. Chem. C. 115 (2011) 14392–14399.

[27] S. Chen, J. Zhu, X. Wu, Q. Han, X. Wang, Graphene oxide− MnO_2 nanocomposites for supercapacitors, ACS Nano. 4 (2010) 2822–2830.

[28] A. Bello, F. Barzegar, D. Momodu, J. Dangbegnon, F. Taghizadeh, N. Manyala, Symmetric supercapacitors based on porous 3D interconnected carbon framework, Electrochim. Acta. 151 (2015) 386–392.

[29] B. Abdulhakeem, B. Farshad, M. Damilola, T. Fatemeh, F. Mopeli, D. Julien, N. Manyala, Morphological characterization and impedance spectroscopy study of porous 3D carbons based on graphene foam-PVA/phenol-formaldehyde resin composite as an electrode material for supercapacitors, RSC Adv. 4 (2014) 39066.

[30] K.V. Sankar, D. Kalpana, R.K. Selvan, Electrochemical properties of microwave-assisted reflux-synthesized Mn_3O_4 nanoparticles in different electrolytes for supercapacitor applications, J. Appl. Electrochem. 42 (2012) 463–470.

[31] T. Gao, H. Fjellvåg, P. Norby, A comparison study on Raman scattering properties of α- and β-MnO_2, Anal. Chim. Acta. 648 (2009) 235–239.

[32] A.C.A. Ferrari, Raman spectroscopy of graphene and graphite: disorder, electron-phonon coupling, doping and nonadiabatic effects, Solid State Commun. 143 (2007) 47–57.

[33] K. Fic, G. Lota, M. Meller, E. Frackowiak, Novel insight into neutral medium as electrolyte for high-voltage supercapacitors, Energy Environ. Sci. 5 (2012) 5842.

[34] H. Gao, F. Xiao, C.B. Ching, H. Duan, High-Performance Asymmetric Supercapacitor Based on Graphene Hydrogel and Nanostructured MnO_2, ACS Appl. Mater. Interfaces. 4 (2012) 2801–2810.

[35] Y. Dai, J. Li, G. Yan, G. Xu, Q. Xue, F. Kang, Preparation of the cactus-like porous manganese oxide assisted with surfactant sodium dodecyl sulfate for supercapacitors, J. Alloys Compd. 621 (2015) 86–92.

[36] Y. Liu, D. He, H. Wu, J. Duan, Graphene and nanostructured Mn_3O_4 composites for supercapacitors, Integr. Ferroelectr. 144 (2013) 118–126.

[37] F.B. E. Frackowiak, E. Frackowiak, F. Beguin, F. Béguin, Carbon materials for the electrochemical storage of energy in capacitors, Carbon 39 (2001) 937–950.

[38] F.W. Richey, B. Dyatkin, Y. Gogotsi, Y. a Elabd, Ion dynamics in porous carbon electrodes in supercapacitors using in situ infrared spectroelectrochemistry. J. Am. Chem. Soc. 135 (2013) 12818–26.

[39] F. Béguin, V. Presser, A. Balducci, E. Frackowiak, Carbons and electrolytes for advanced supercapacitors., Adv. Mater. 26 (2014) 2219–51, 2283.

[40] D.P. Dubal, D.S. Dhawale, R.R. Salunkhe, C.D. Lokhande, Conversion of chemically prepared interlocked cubelike Mn3O4 to birnessite MnO2 using electrochemical cycling, J. Electrochem. Soc. 157 (2010) A812–A817.

[41] S.W. Lee, J. Kim, S. Chen, P.T. Hammond, Y. Shao-Horn, Carbon nanotube/manganese oxide ultrathin film electrodes for electrochemical capacitors, ACS Nano. 4 (2010) 3889–3896.

[42] S.-B. Ma, K.-Y. Ahn, E.-S. Lee, K.-H. Oh, K.-B. Kim, Synthesis and characterization of manganese dioxide spontaneously coated on carbon nanotubes, Carbon 45 (2007) 375–382.

[43] L. Bao, J. Zang, X. Li, Flexible Zn_2SnO_4/MnO_2 core/shell nanocable- carbon microfiber hybrid composites for high-performance supercapacitor electrodes, Nano Lett. 11 (2011) 1215–1220.

[44] S. Nagamuthu, S. Vijayakumar, G. Muralidharan, Synthesis of Mn_3O_4 / Amorphous Carbon Nanoparticles as Electrode Material for High Performance Supercapacitor Applications, Energy & Fuels. 27 (2013) 3508–3515.

[45] Y.-T. Wang, A.-H. Lu, H.-L. Zhang, W.-C. Li, Synthesis of Nanostructured Mesoporous Manganese Oxides with Three-Dimensional Frameworks and Their Application in Supercapacitors, J. Phys. Chem. C. 115 (2011) 5413–5421.

[46] V. Khomenko, E. Raymundo-Pinero, E. Frackowiak, F. Beguin, High-voltage asymmetric supercapacitors operating in aqueous electrolyte, Appl. Phys. A. 82 (2006) 567–573.

[47] E.C. Rios, A. V Rosario, R.M.Q. Mello, L. Micaroni, Poly (3-methylthiophene)/MnO_2 composite electrodes as electrochemical capacitors, J. Power Sources. 163 (2007) 1137–1142.

[48] S. Faraji, F.N. Ani, Microwave-assisted synthesis of metal oxide/hydroxide composite electrodes for high power supercapacitors-A review, J. Power Sources. 263 (2014) 338–360.

[49] F. Shi, L. Li, X. Wang, C. Gu, J. Tu, Metal oxide/hydroxide-based materials for supercapacitors, RSC Adv. 4 (2014) 41910–41921.

[50] B.G. Choi, J. Hong, W.H. Hong, P.T. Hammond, H. Park, Facilitated ion transport in all-solid-state flexible supercapacitors, ACS Nano. 5 (2011) 7205–7213.

[51] Y.-R. Nian, H. Teng, Nitric acid modification of activated carbon electrodes for improvement of electrochemical capacitance, J. Electrochem. Soc. 149 (2002) A1008–A1014.

[52] J. Zhang, J. Jiang, X.S. Zhao, Synthesis and capacitive properties of manganese oxide nanosheets dispersed on functionalized graphene sheets, J. Phys. Chem. C. 115 (2011) 6448–6454.

[53] M. Pasta, F. La Mantia, L. Hu, H.D. Deshazer, Y. Cui, Aqueous supercapacitors on conductive cotton, Nano Res. 3 (2010) 452–458.

[54] E. Lust, A. Jänes, M. Arulepp, Influence of solvent nature on the electrochemical parameters of electrical double layer capacitors, J. Electroanal. Chem. 562 (2004) 33–42.

[55] D. Pech, M. Brunet, H. Durou, P. Huang, V. Mochalin, Y. Gogotsi, P-L. Taberna, P. Simon, Ultrahigh-power micrometre-sized supercapacitors based on onion-like carbon., Nat. Nanotechnol. 5 (2010) 651–654.

[56] M. Biswal, A. Banerjee, M. Deo, S. Ogale, From dead leaves to high energy density supercapacitors, Energy Environ. Sci. 6 (2013) 1249–1259.

[57] M. Sluyters-Rehbach, Impedances of electrochemical systems: Terminology, nomenclature and representation-Part I: Cells with metal electrodes and liquid solutions (IUPAC Recommendations 1994), Pure Appl. Chem. 66 (1994) 1831–1891.

[58] Y. Zhou, H. Xu, N. Lachman, M. Ghaffari, S. Wu, Y. Liu, A. Ugur, K.K. Gleason, B.L. Wardle, Q.M. Zhang, Advanced asymmetric supercapacitor based on conducting polymer and aligned carbon nanotubes with controlled nanomorphology, Nano Energy. 9 (2014) 176–185.

Supporting information

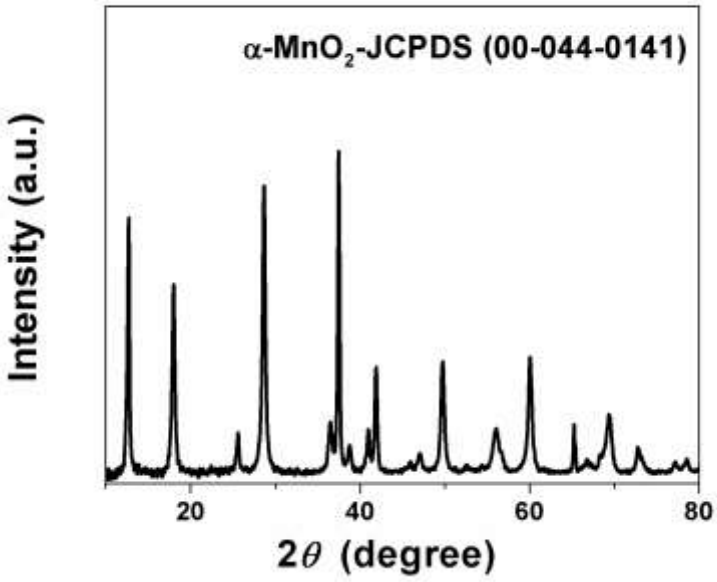

Figure S1. XRD pattern of as-syntheisized α-MnO_2 nanoparticles.

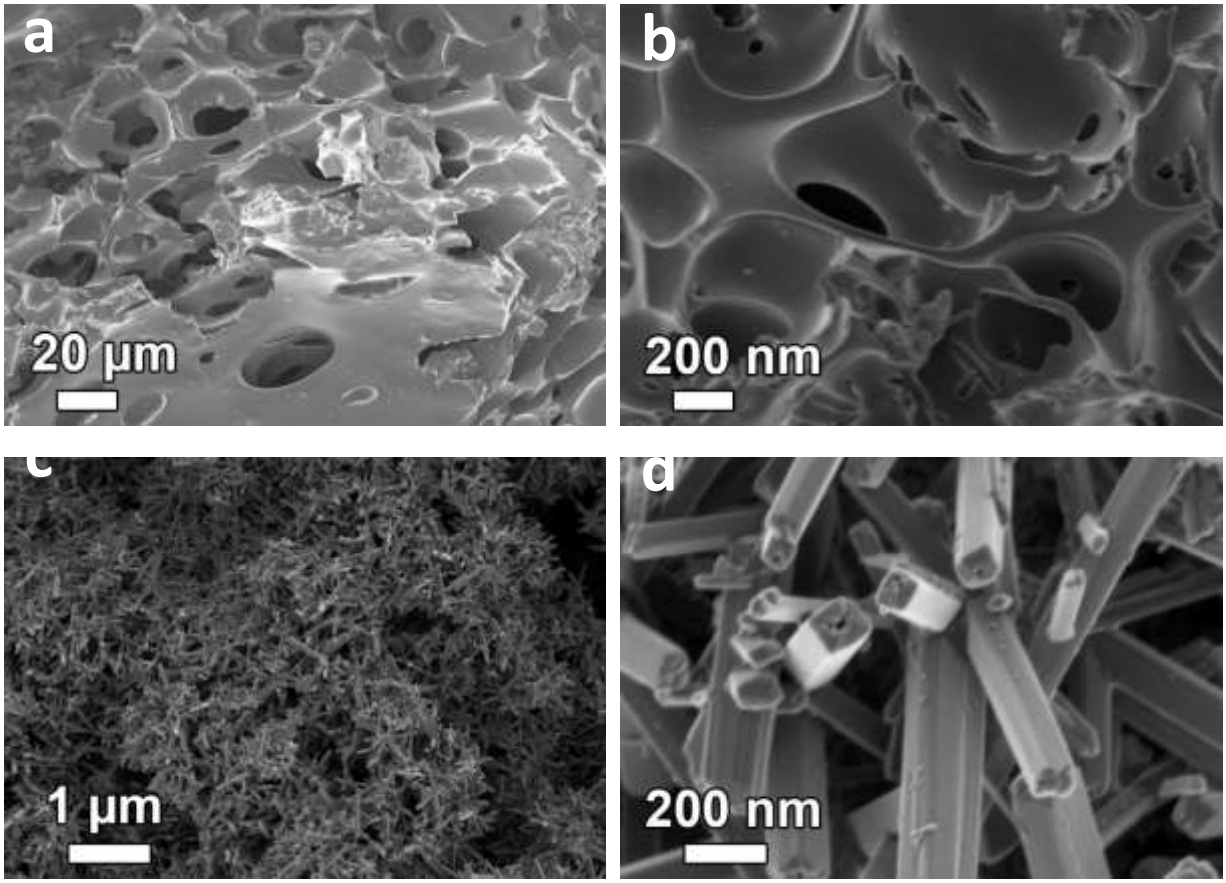

Figure S2. FESEM of (a, b) the activated carbon and (c,d) the α-MnO_2.

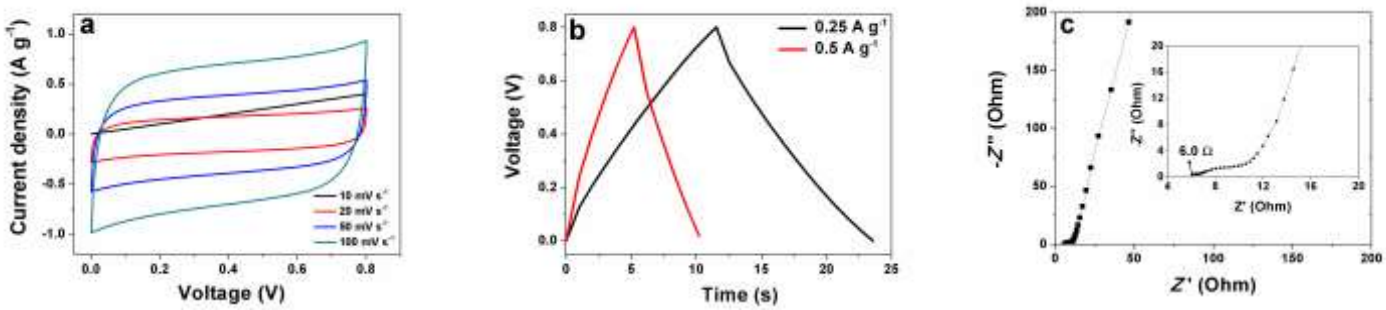

Figure S3. (a) CV, (b) CD and (c) EIS plots of the α-MnO_2 nanostructure over potential window of 0.8 V.

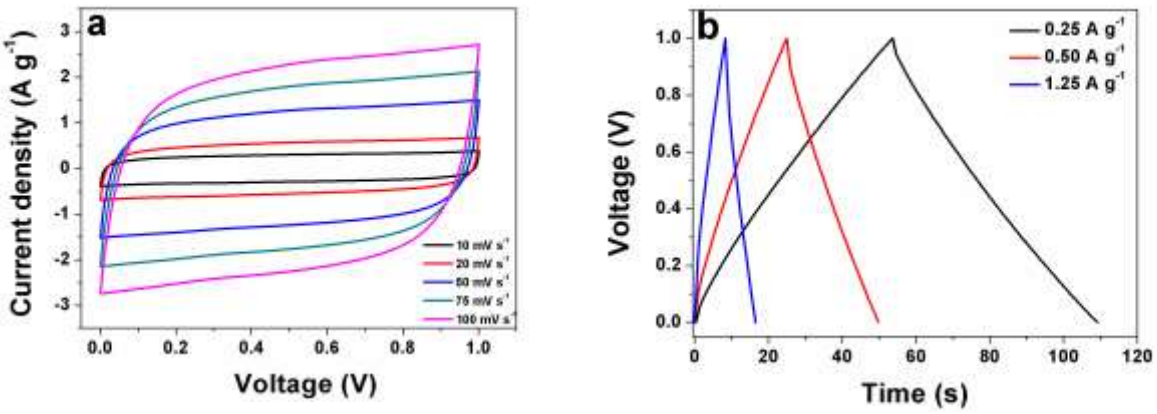

Figure S4. (a) CV at different scan rate and (b) CD at differen current density of AC-Mn_3O_4.

Table S1 showing electrochemical result for the three samples produced

Catalyst	**C_{sp} /F g^{-1}**	**E_{max} /Wh kg^{-1}**	**P_{max} / W kg^{-1}**
α –MnO_2	21.1	-	-
AC-Mn_3O_4	55.3	2.3	0.60
AC-MnO_2	180	7.53	0.2